# Development and Testing of a Multilevel Chevron Actuator-Based Positioning System

Sahil Oak, Sandesh Rawool, Ganapathy Sivakumar, Egbert J. Hendrikse, Jr., Daniel Buscarello, and Tim Dallas, *Member, IEEE*

***Abstract*—We present the design, fabrication, and testing of a microscale positioning system. The system was designed in the SUMMiT V process to produce in-plane, bidirectional, micrometer-scale linear motion of a shuttle using a ratcheting mechanism and multilayered chevron actuators. A single latching system with oppositely faced ratchet teeth on either side of the shuttle is used for achieving the bidirectional actuation. The device has a smaller footprint and fewer electrical connections compared to similar devices, without compromising performance. Moreover, this device is capable of generating more force compared to previous devices. A LabVIEW-based optical characterization setup was developed for automated testing of the device. The device produced a maximum displacement of $\sim$180 $\mu$m with a step size of 9 $\mu$m. [2011-0151]**

***Index Terms*—Bent-beam actuators, buckling, electro-thermal, microelectromechanical systems (MEMS), micro-actuators, micro-positioning, polysilicon, SUMMiT V.**

## I. Introduction

THE DEVELOPMENT of linear actuators has made possible microelectromechanical systems (MEMS) devices for micro/nanopositioning, biological cell probing, and neural interfaces [1], [2]. There are always tradeoffs between minimum and maximum displacement, force, and degrees of freedom to be considered while developing such systems. For instance, fiber-optical switches typically require long travel ranges, as the fiber diameter is typically 125 $\mu$m (required travel range is at least $\pm$62.5 $\mu$m with enough force to move a silica fiber with 125 $\mu$m [3]. On the other hand, a biological cell probing system requires more precise movement of the actuator with enough force to pierce the cell. Overall, high resolution, relatively large travel range and force are all necessary for micro-actuators to be used for precise positioning.

A variety of MEMS actuators such as magnetic [4], electrostatic [5]–[12], electrothermal [13]–[20], and piezoelectric [8] have been used for producing motion at the micro- and nanometer scales and have been fabricated using surface-micromachined fabrication techniques. While surface micromachined electrostatic actuators, such as the parallel plate or the interdigitated comb-drive style can exert an output force in the tens of micro-Newtons and provide reasonable displacement under resonance, they require a relatively high actuation voltage, and the static displacement under nonresonant conditions can be much lower. Piezoelectric actuators are usually large and require high actuation voltage. Furthermore, it is difficult to get these actuators constructed by the micromachining processes offered by commercial MEMS foundries. Thermal actuators have proven to be a robust actuation method in surface micromachined MEMS processes. They generate a large output force and a larger displacement up to 10.5 mN and 200 $\mu$m, respectively, at comparatively low actuation voltages, which make them an attractive alternative to more traditional electrostatic actuation methods [21]. The electrothermal actuators use resistive (Joule) heating to generate thermal expansion resulting in movement. In spite of all these advantages, making use of these actuators alone does not provide the entire solution, when displacements in the range of hundreds of micrometers are required. In addition, it is advantageous for the actuator to hold position with minimum power requirements, i.e., zero-power latching. This reduces energy consumption while making them robust against power interruptions. By combining thermal actuators as part of the system along with a compliant mechanism, more complex systems can be built, and the number of possible applications in which they are used increases dramatically.

Kolesar *et al.* [22] demonstrated a MEMS micro-engine using arrays of surface micromachined asymmetrical electrothermal micro-actuators. They obtained an in-plane movement spanning 1–10 $\mu$m with 8 $\mu$N force from individual micro-actuators. de Boer *et al.* [23] developed a surface micromachined inchworm actuator that is capable of producing bidirectional motion with a maximum displacement of

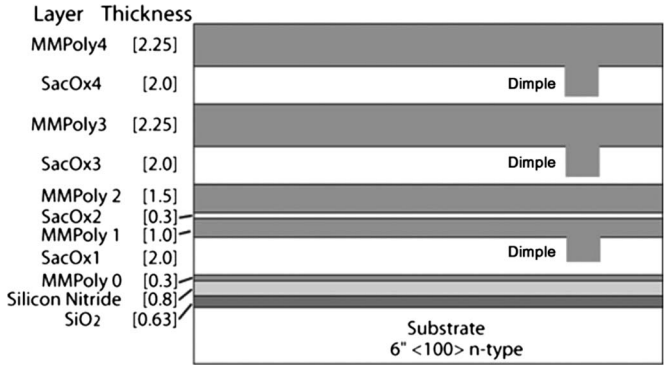


Fig. 1. Cross-sectional view of the SUMMiT V process layers. Thicknesses in micrometers of each layer are given in the parenthesis [26].

Manuscript received May 18, 2011; revised July 27, 2011; accepted August 6, 2011. Date of publication October 6, 2011; date of current version December 2, 2011. This work was supported by the Welch Foundation (D-1651) and by the National Science Foundation (EEC-0648761, DUE-0837521, IIP-1014222). Subject Editor Y. B. Gianchandani.

The authors are with the Electrical and Computer Engineering, Texas Tech University, Lubbock, TX 79409 USA (e-mail: s.oak@ttu.edu; s-rawool@ti.com; s.ganapathy.s@gmail.com; johan.hendrikse@gmail.com; kemsyko@gmail.com; tim.dallas@ttu.edu).

Color versions of one or more of the figures in this paper are available online at http://ieeexplore.ieee.org.

Digital Object Identifier 10.1109/JMEMS.2011.2167674

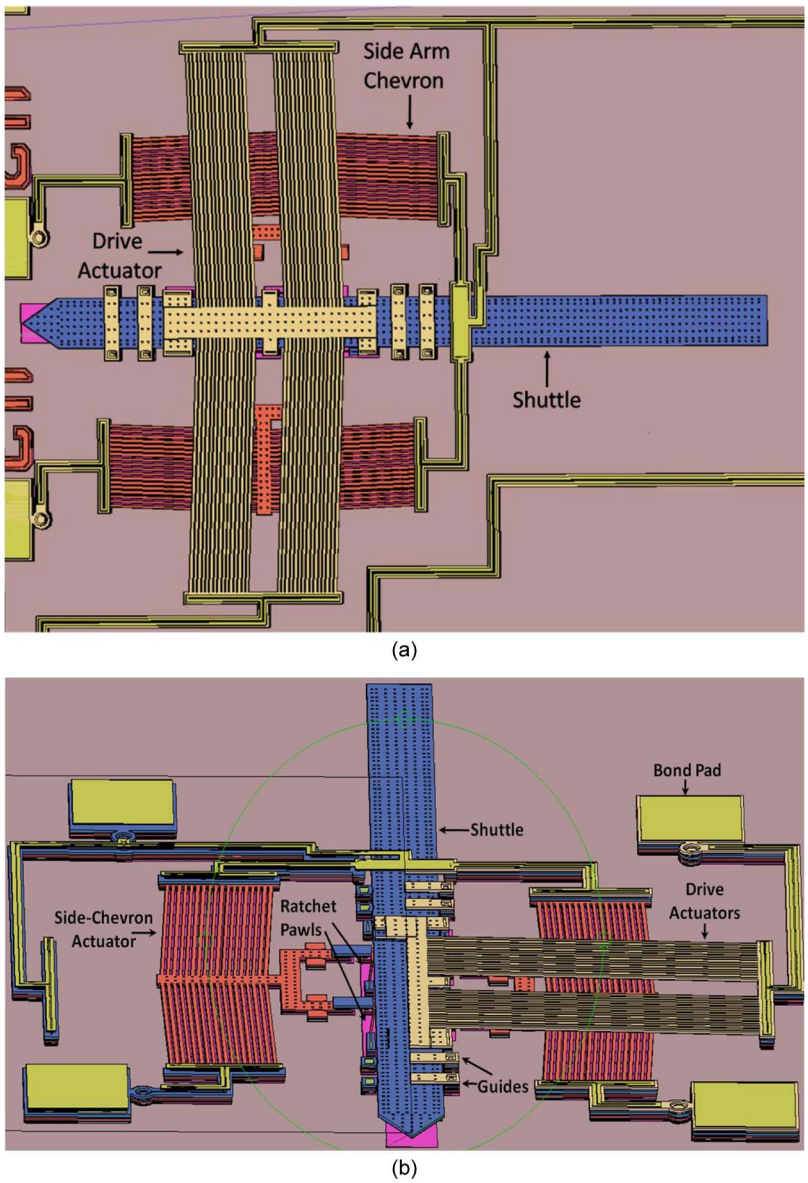


Fig. 2. (a) 3-D model of the device consisting of two side arm actuators, drive actuator, and shuttle. (b) AutoCAD 3-D cut view of the device highlighting the ratcheting system.

$\pm 100$ $\mu$m and $\pm 0.5$ mN force. Shutov *et al.* [24] demonstrated an electrostatic inchworm microsystem with adjustable step size of 0.05 to 2 $\mu$m and operating voltage of around 120 V. Toda *et al.* [25] produced a normally latched, large stroke inchworm microactuator with an actuation stroke of 600 $\mu$m with the comb drives operating at around 200 V. Muthuswamy *et al.* [1] developed positionable microelectrodes for monitoring neuronal activities in rodent brains. This device used an electrostatic rotational drive, coupled to a linear rack to achieve a bidirectional motion of 2 mm with a step resolution in the order of 1 $\mu$m. Another design they have demonstrated incorporated electrothermal bent beam actuators to obtain a bidirectional motion of 2–3 mm with a step size of 8.8 $\mu$m [1], [2].

In this work, we present the development and testing of a microscale positioning system. The device allows in-plane, bidirectional, linear motion of a shuttle in discrete steps of $\sim 9$ $\mu$m using a counter ratcheting mechanism and multilevel chevron actuators built using the SUMMiT V fabrication process. The design is intended to reduce the footprint and number of electrical connections needed, compared to similar devices [1]. Finite-element analysis (FEA) software (ANSYS) was used to simulate the electrothermal actuators with a coupled structural-thermal model. The fabricated system was tested using a custom built optical characterization setup controlled using National Instruments LabVIEW software. The tests are performed to determine the functional parameters of the device in both the forward and reverse directions and also to determine if any skips or multiple ratcheting events occur during operation.

## II. Design and Fabrication

The design and fabrication of the device were done using the standard SUMMiT V (**S**andia's **U**ltra-planar **M**ultilevel **M**EMS **T**echnology) process from Sandia National Laboratories (Albuquerque, NM). Fig. 1 shows the cross-section view

of the various structural and sacrificial layers available in the SUMMiT V process along with their thickness in [micrometers]. The process consists of four mechanical layers of polysilicon (*Poly1–Poly4*) above a thin, highly doped polysilicon layer (*Poly0*) which can be used for electrical interconnect and as a ground plane. The structural layers are separated by a total of four sacrificial oxide layers (*SacOx1–SacOx4*) [26].

Fig. 2(a) shows the 3-D view of the AutoCAD-based design. The device is comprised of three important components namely, the central shuttle, ratcheting system, and the side guides. The central shuttle is the basic component of the device which is $64\ \mu\text{m} \times 1,018\ \mu\text{m}$. It is a free moving structure located beneath the drive actuator (DA) and between the two side chevron actuators. It is composed of the *Poly1/Poly2 laminate* and the *Poly3* layer. The *Poly3 and Poly2* layers are attached using multiple *SacOx3* cuts. There are oppositely facing serrated teeth on either side of the shuttle which are used for its movement in the forward and reverse directions, when meshed with the ratchet pawls. The teeth have a pitch size of 9 $\mu$m, as shown in Fig. 3, which defines the digital step size of the device. The shuttle also has *Poly1*, *Poly2*, and *Poly3* cuts of $2\ \mu\text{m} \times 2\ \mu\text{m}$ which act like etch release holes, so that the sacrificial material below these layers is completely removed, and a free moving structure is obtained. There are dimples beneath the *Poly1* layer obtained using *Dimple1* cuts so that the contact area between the shuttle and *Poly0* layer is minimized, thus reducing stiction. The ratcheting system shown in Fig. 2(b) is an important part of the device since it incorporates all the mechanism for the device operation. It consists of the top chevron actuator (DA), ratcheting pawls, and the side chevron actuators. The DA is an overhanging structure built at the *Poly4* layer, which allows it to move without any obstruction. It holds the ratchet pawls on either sides of the shuttle, as shown in Fig. 3. A *SacOx4* cut enables connection between the *Poly4* layer and the *Poly3* layer. Another *SacOx3* cut is made to attach the *Poly 3* layer to the *Poly2* layer. The DA is powered using a separate bond pad and a common ground. It is designed to provide enough force and displacement to slide the pawls on the teeth and move the shuttle in both directions depending on the set of ratchet pawls engaged onto the shuttle.

The ratchet pawls are compliant structures composed of the *Poly 1/Poly 2* laminate. There are two different types of ratchet pawls used on either sides of the shuttle, one anchored to the *Poly 0* layer and the other attached to the *Poly 4* DA [Fig. 4(c)]. The pawls attached to the DA are responsible for moving the shuttle while the pawls which are anchored hold the shuttle in place and prevent any unwanted movement of the shuttle. Also, the pawls are mechanically coupled to the side arm actuators using a pin type structure. A 2-D cross section of the ratchet pawl is shown in Fig. 4(d). It has a rectangular slot in it, which is made using a *Poly2* cut which allows it to be free to move in the direction of the DA when the pawl is engaged to the shuttle, whereas the pawl can be retracted backwards to disengage from the shuttle using the side arm actuators as the distance between slot edge and the pin is kept to be 1 $\mu$m.

The side chevron actuators are constructed using the *Poly1/Poly2 laminate* layer which allows for the thicker chevron arms, thus increasing the aspect ratio and minimizing any out-of-plane motion of the actuator. It has a special U-shaped structure connected to the middle arm which helps in engagement and disengagement of the ratchet pawls. Two bridge-type structures on the *Poly3* layer extend from the side chevrons to the ratchet pawl, and the coupling between them is attained using dimples at the *Poly1* layer. There is a similar system on the other side of the shuttle for engaging and disengaging the pawls on the other side. Both the side arm actuators have different bond pads for electrical connection, but share a common ground. The shuttle is held in place by four guides; two located at the front, and two at the back, as shown in Fig. 5(a). The guide consists of two anchors on both sides of the shuttle *Poly0–Poly3* layers with the *Poly4* layer connecting these anchors forming a bridge-type structure. The function of the guides is to minimize any in-plane nonlinear movement of the shuttle and also to minimize any out-of-plane movement, thus making it more reliable and producing linear motion. There is a notch made on the shuttle, as shown in Fig. 5(c), such that initial spacing between the shuttle and guide is 1 $\mu$m, but once it moves forward or backward by one step, this spacing reduces to 0.25 $\mu$m. There are four side stops, two in the front, and two at the back to reduce any nonlinear motion of the DA. These stops help keep the DA in position and prevent the DA from getting pulled sideways by the side chevron actuator when engaging and disengaging the pawls.

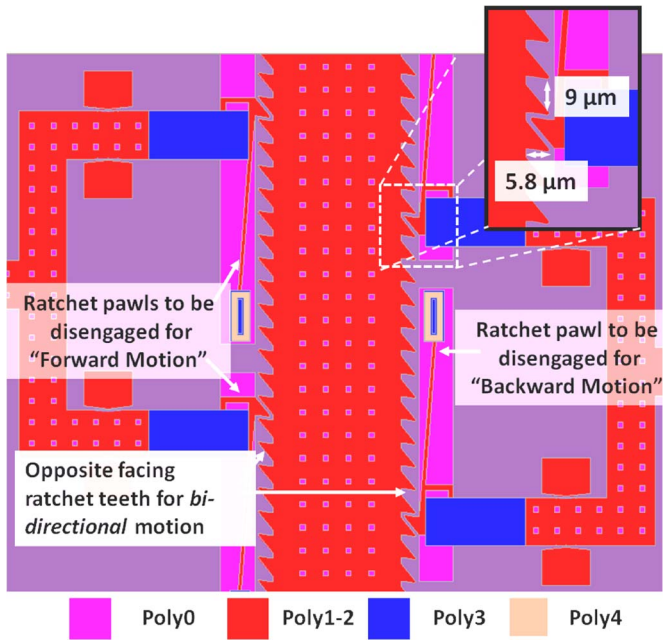


Fig. 3. Three-dimensional model of the central shuttle with ratchet pawls, showing opposite facing serrated teeth along with their dimensions.

## III. Device Operation

The system is driven by a combination of electrothermal chevron actuators and a ratcheting mechanism. A central shuttle with oppositely facing ratchet teeth helps attain bidirectional motion using two different sets of chevron actuators viz.: 1) Side chevron actuators, one on each side; and 2) Top chevron actuator, coupled to a counter ratcheting system. The direction

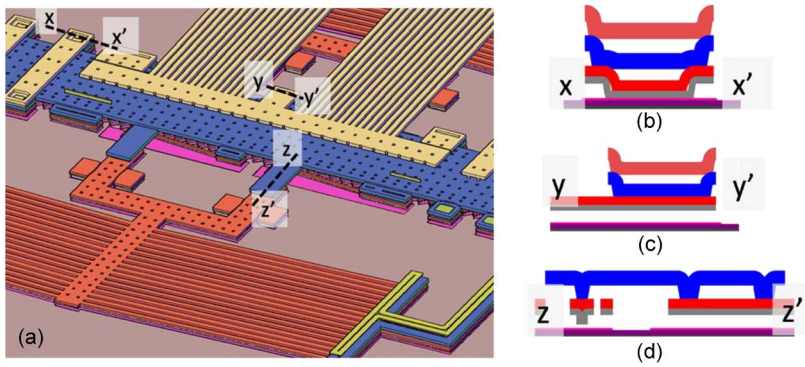


Fig. 4. (a) 3-D cut model of the device showing the two types of ratchet pawls and their coupling with the side chevron actuator. (b) 2-D cross-section view of the anchored ratchet pawl. (c) 2-D cross-section view showing the second ratchet pawl attached to the drive actuator. (d) 2-D cross-section view of the ratchet pawl coupled to the extended chevron arm.

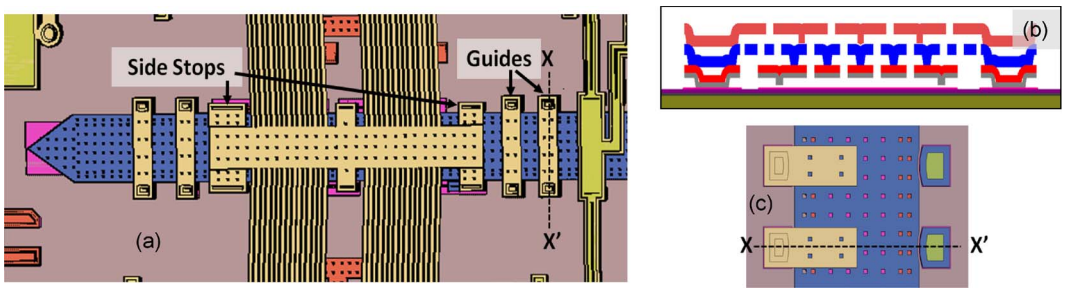


Fig. 5. (a) 3-D model of the device showing the guides and side stops. (b) 2-D cross-section view showing guides on the side of the shuttle. (c) 3-D view showing the notch on the shuttle to compensate for the 1 $\mu$m gap due to minimum feature size of the process.

of motion of the shuttle depends on which side chevron actuator is powered "ON," thus engaging or disengaging the ratchet pawls on respective sides. The serrated teeth on both sides of the shuttle and the shapes of the ratcheting pawls are designed such that the right side of the system allows shuttle motion in the forward direction, whereas the left side allows reverse motion.

Fig. 6 illustrates the operation sequence of the system for the forward motion of the shuttle. Event (a) shows the initial position of the system at power down. In Event (b), the Left Side chevron actuator is powered "ON," which disengages both the ratchet pawls on that side. The shuttle is free to move in the forward direction. In Event (c), the DA is powered "ON" which pulls back one of the ratchet pawl (attached to the *Poly4* structure) on the right, while the second pawl (attached to the substrate) still holds the shuttle, thus preventing any reverse motion. Also, the shuttle teeth and the pawls are designed such that the pawl slides out and ratchets to the next tooth. In Event (d), when powering "OFF," the DA returns to its original position and takes the shuttle along with it, one step forward due to engagement of the ratchet pawls on the right. In this event, the fixed pawl, locking the movement of the shuttle, slides out and ratchets onto the next tooth, thus ensuring that at any particular event, one of the four pawls holds the shuttle in place. In Event (e), the left side chevron actuator is powered "OFF" if no further step motion is required. The whole sequence of operation is for one step increment of the shuttle and needs to be repeated for additional displacement.

Similarly, for reverse motion of the shuttle, all the sequences are repeated except that the chevron actuator on the right side is powered "ON," which disengages the pawls on that side and allows for reverse motion. This drive mechanism allows for actuation of the shuttle in both directions with only three relatively simple drive signals and a ground. The unit step motion is determined by the stroke of the DA and the separation of the ratchet teeth on the shuttle. This actuator is capable of zero-power latching, that is, the shuttle maintains its position when the power is turned "OFF."

## IV. Modeling and Actuator Optimization

Electrothermal actuators are preferred in applications where there is a need for larger force ($> 10$ $\mu$N) and greater displacements ($> 10$ $\mu$m). These actuators have large energy densities allowing them to be more compact in comparison to other actuators. These devices have a significant disadvantage of having low efficiency and hence cannot be used in low-power applications. Keeping all these characteristics in mind, design and optimization of actuators are essential. The three most important things modeled were: the side arm actuators, the ratchet pawls, and the DA.

The actuators are modeled for the dimensions listed in Fig. 7 using FEA ANSYS which is capable of performing nonlinear analysis. The polysilicon structure was modeled as a 20-node brick element (226), with a Poisson's ratio of 0.22 and a Young's modulus of $1.69 \times 10^{11}$ N/m$^2$ ($169 \times 10^3$ in $\mu$MKS). The electrothermal actuators work on the principle of Joule heating, which leads to beam expansion, and, thus, linear displacement is obtained. The purpose of this analysis is to predict the maximum displacement attained by the actuator as a function of voltage and temperature. This will also give an

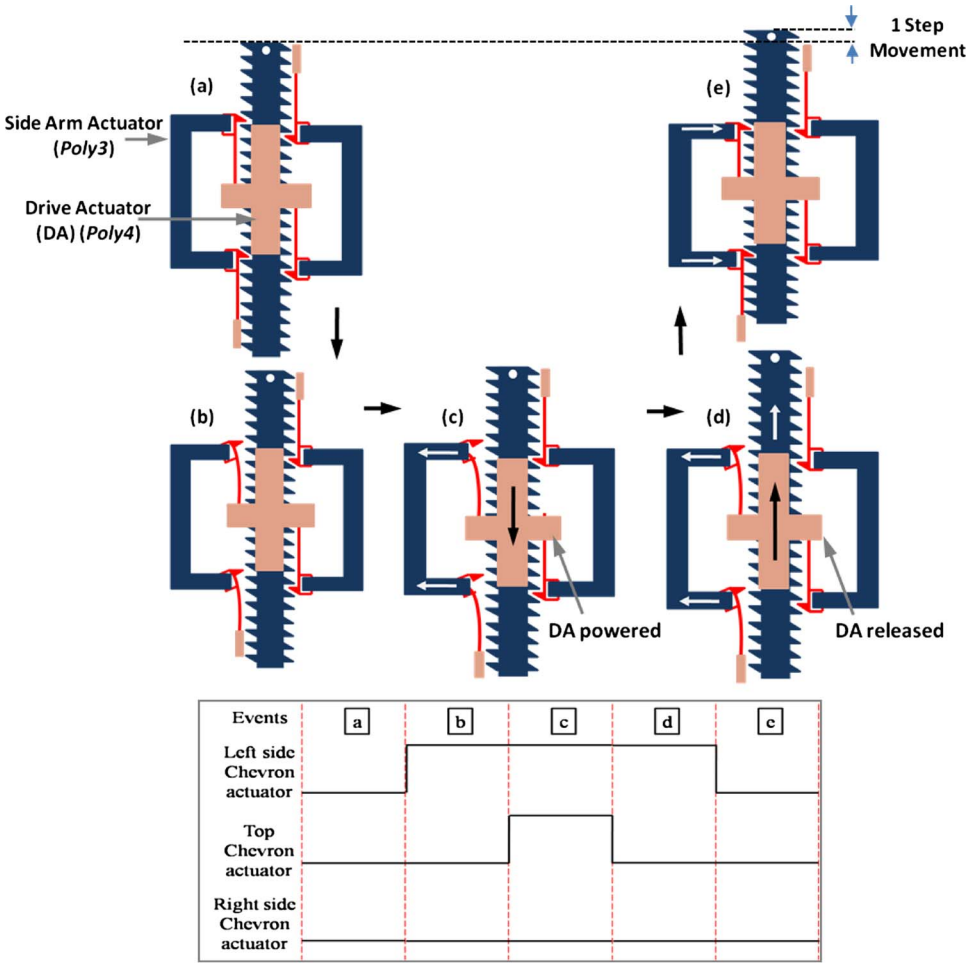


Fig. 6. (a) Events to move the shuttle one step in the forward direction. (b) Sequence of pulses given to the chevron actuators during forward motion.

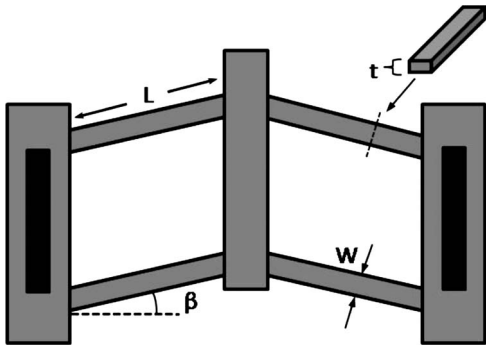


Fig. 7. Illustration showing dimensions for the bent beam actuators used in the design.

idea if the actuators are working in the preferable elastic regime to give the required displacement or entering the plasticity regime wherein it is difficult to recover to the same zero-power position. It is assumed that the substrate does not expand since the input power is very low and hence was not considered in the analysis. The anchors were constrained for temperature conditions at room temperature (30 °C) which means the primary heat loss from the beam is to the surrounding ambient and not transferred to the anchors.

The side arm actuators are designed to engage/disengage the ratchet pawls from the central shuttle. This *Poly1/Poly2*

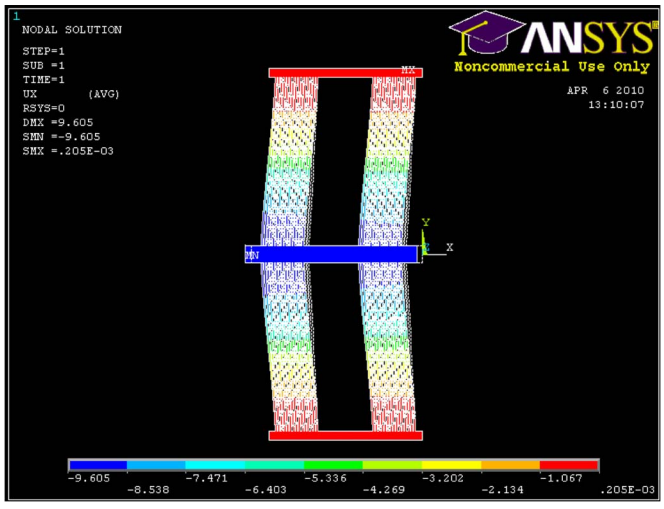


Fig. 8. FEA simulation showing displacement along X-axis showing maximum displacement of 9.6 $\mu$m.

*laminate* actuator needs displacement of at least 6 $\mu$m and to generate enough force to pull out the ratchet pawl and completely disengage it from the shuttle. As shown in Table I, the optimum parameters for this design were found out to be a length of 200 $\mu$m, width of 3.5 $\mu$m, and thickness of 2.5 $\mu$m at a bend angle of 2°. The ratchet pawls were modeled to be

compliant enough to be pulled by the actuation of the side arm actuator as well as to allow bending, while the tooth on the shuttle slides over the pawl to engage the next tooth without generating significant disorientation in the shuttle motion. FEA modeling and design optimization were done by doing a contact analysis. The upper end of the pawl was modeled as a contact surface with the DA. The lower end of the pawl is attached to the substrate constrained in the X, Y, and Z axes. The load on the pawl is simulated by application of the voltage to provide the required displacement of 9 $\mu$m to the DA. The Von Mises stress for the pawl was observed for all the actuation voltages and was found to be well below the fracture limits. The length and width of the pawl were kept at 56 $\mu$m and 1.5 $\mu$m, respectively. The DA was designed to provide the shuttle bidirectional movement. It needs to move the *Poly4* structure so that the attached *Poly2* ratchet pawls slides over the current teeth engagement and engages the next tooth. The size of a tooth is 9 $\mu$m. Hence, the actuator should displace by this distance and generating enough force to move attached shuttle along with it. The maximum loading force is generated by a bent-beam actuator at the apex $f_{\max}$ and could be calculated using a formula derived by the complimentary energy method [17]

$$f_{\max} = d_{\max}.K_y; \qquad K_{\mathrm{y}} = \frac{4\sin^2(\beta)AE}{2L\cos\beta} \tag{1}$$

where $A = Wt$ is the cross-sectional area of the beam, and $\beta'$ is the bending angle. The formula is validated by comparing the results of the FEA. It was found that the theoretical force values calculated by (1) were almost the same as that given by the FEA simulation results. For FEA analysis, the force was calculated by summing the forces at a midpoint on the front face of the middle arm. Using formula (1), $\beta = 0.034'$, $L = 325$ $\mu$m, $A = 2.25 \times 3.5 = 7.9$ $\mu$m$^2$, and $E = 164.3$ GPa $\pm$ 3.2 GPa [27] for $d_{\max}$ of 10 $\mu$m, we found the force generated by one arm to be 92 $\mu$N and for 30 arms, the force totals 2.76 mN $\pm$ 50 $\mu$N. The result obtained is within 5% of the force values obtained from the FEA simulations for the Drive Chevron actuator.

From the FEA results, it is observed that the DA attains this displacement at 630 °C which is below the temperature which polysilicon undergoes permanent creep/significant plastic deformation ($> 800$ °C), whereas the side-arm actuator generates the required displacement below (610 °C), the region where *in situ* annealing can be a threat [28].

## V. Testing and Characterization

Fig. 9 shows an SEM image of the fabricated device. The device comes with a vapor self-assembled monolayer [perfluorodecyltrichlorosilane (FDTS)] coating for reduction of stiction. The overall design size is 1.2 mm by 0.5 mm. The chip on which the device resides is packaged at Sandia National Laboratories in a 48-pin dual in-line package. The large pin count allows numerous devices, including the bidirectional linear actuator to be readily controlled without the need for probes.

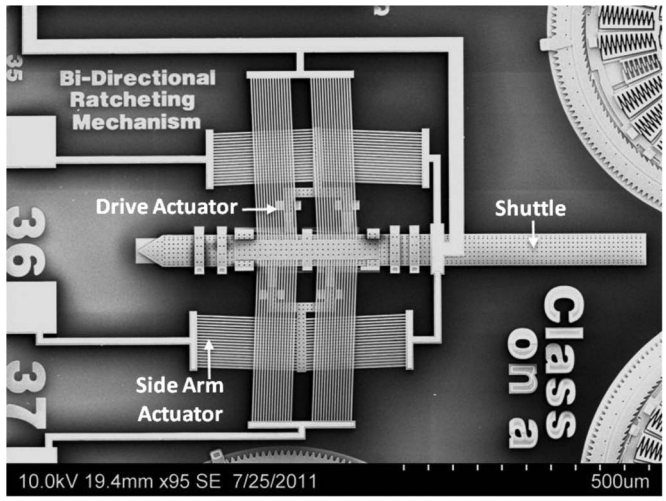


Fig. 9. SEM image of a bidirectional long travel linear actuator.

### A. Measurements of Displacements and Electrical Characteristics of Actuators

Characterization of the thermal actuators is essential to determine their safe operating limits (maximum voltage/current). The optical characterization apparatus consists of an Olympus BX60 System microscope with multiple objectives and a CCD camera to image the device under actuation. The CCD was connected to a computer running LabVIEW through an IMAQ interface. The actuation stimuli to the device under test were provided through a commercial power supply (Keithley 2400). The power supply interface was automated using a LabVIEW virtual instrument (VI) running on the console. The connection between the power supply and the computer was established using a GPIB interface. Further details on the key features involved in the test setup are provided in the subsequent subsections.

*1) Characterization of Side Actuator:* The characterization of the side actuator involved creating a LabVIEW VI that was used to source the current at the given compliance voltage of 40 V in 1 mA increments from 0 to 90 mA. The VI also consists of a frame grabber and a read routine. The frame grabber was programmed to capture images and store them at specified location on a local disk. The read routine logs the voltage measured across the actuator (device under test—DUT) into an Excel file which was later used to calculate the power consumption. National Instruments Vision Builder Software was used to process the images and then measure the displacement at each 1 mA increment. The images were captured with a 50X objective (0.50 NA). At 50X, a pixel error of $\pm 0.1$ $\mu$m is determined for the setup.

In all, five devices were tested. Each device has two sets of side arm actuators allowing ten actuators total to be tested. The graph shown in Fig. 10 displays the plot of calibrated displacement with respect to applied current. It shows that for a displacement of 5.5 $\mu$m, a current of 63 mA (average of 10 readings) is needed for complete disengagement of the ratchet pawls. This actuator could be operated in the range of 63–70 mA (elastic regime). After 75 mA, the polysilicon starts to develop permanent creep.

TABLE I
TABLE SHOWING DIMENSIONS FOR THE BENT-BEAM ACTUATORS USED IN THE DESIGN

| | Side Arm Actuator | Drive Actuator |
|---|---|---|
| Length of the beams (L) | 200 µm | 325 µm |
| Width of the beams (W) | 3.5 µm | 3.5 µm |
| Angle of the beams (β) | 2° | 2° |
| Layer thickness (t) | 2.5 µm | 2.5 µm |
| Total number of beams | 18 | 30 |
| Function | Engage/Disengage pawls | Drives the shuttle |

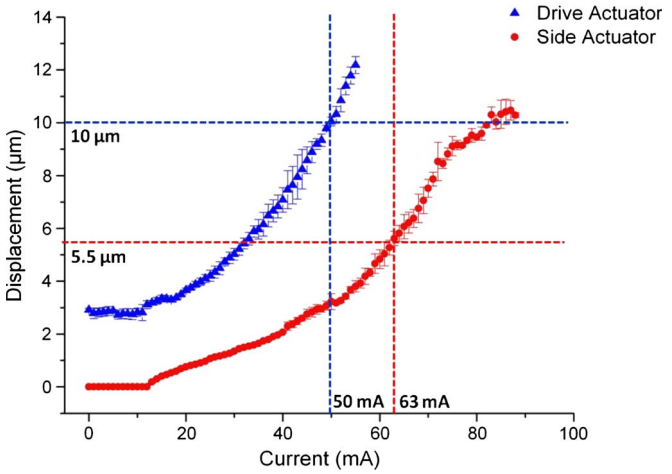


Fig. 10. Plot of current versus displacement for the side arm actuator and drive actuator.

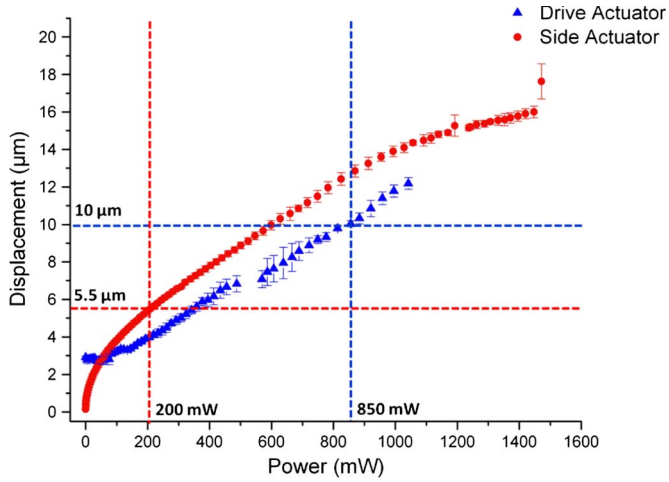


Fig. 11. Plot of power versus displacement for side arm actuator and drive actuator.

*2) Characterization of Drive Actuator:* The drive chevron was characterized over a series of steps which was automated using a LabVIEW VI. First, both the side arm actuators are powered so that the central shuttle is free to move. The DAs are then actuated, and the position is captured using the frame grabber. The read routine is employed to measure the voltage across the actuator. After the data acquisition (DAQ), the DA is powered down, and pawls are then released to engage the shuttle again.

Based on the previous results, 63 mA was passed through each side actuator so that the pawls disengaged. It was observed that there is about 3 $\mu$m of initial displacement in the drive chevron without actuation. The voltage across it was measured using a multimeter and was found out to be 4.8 V. This electrical crosstalk between the three actuators is attributed to the common bond-pad connection which is used to sink the currents (ground) for both the side actuators and DA. A plot of displacement as a function of current shows that the required 10 $\mu$m of displacement is achieved at 50 mA. Fig. 11 shows the plot of displacement versus power. The total power while operating the device is the summation of power to both actuators which is 1.05 W.

## B. Device Characterization

After determining the optimum values for the operation of individual actuators, we actuated this device by executing the sequence of operations for both forward and reverse motion of the shuttle through automated testing using a LabVIEW VI. Two National Instrument's DAQ Hardware (USB 6259) boards were used to generate the pulses at a user-defined frequency and duty cycle. Using the VI, these two boards were synchronized to obtain a set number of pulses. DAQ pulses act as a drive voltage to the gate of the FETs, which switches the dc input voltage/current from the Keithley source meters (one for each actuator). The output of the switch is then sent to the drive and side actuators at their respective pins. The source meters were set up in the constant-current source mode, and voltage drop is measured across the terminals.

To initiate, the device was driven at a frequency of 1 Hz, and the current-source parameters were kept the same as obtained from the previous tests for optimal device operation (50 mA current for drive and 63 mA for side actuators, respectively). The duty cycles for the side arm actuators and DA were set at 0.50 and 0.10, respectively. The short pulse for the DAs limits the duration of the current going through the bent beam actuators, potentially increasing the reliability of the device. By shortening the "ON" time, we minimize deterioration and prevent deformation of the electrothermal device and thus increase the lifetime of the bent beam actuators in the elasticity regime. The actuator will operate in the linear region for a longer time, increasing the reliability of the device. The rise time for each pulse at the FET output was found out to be 11 $\mu$s. Fig. 12

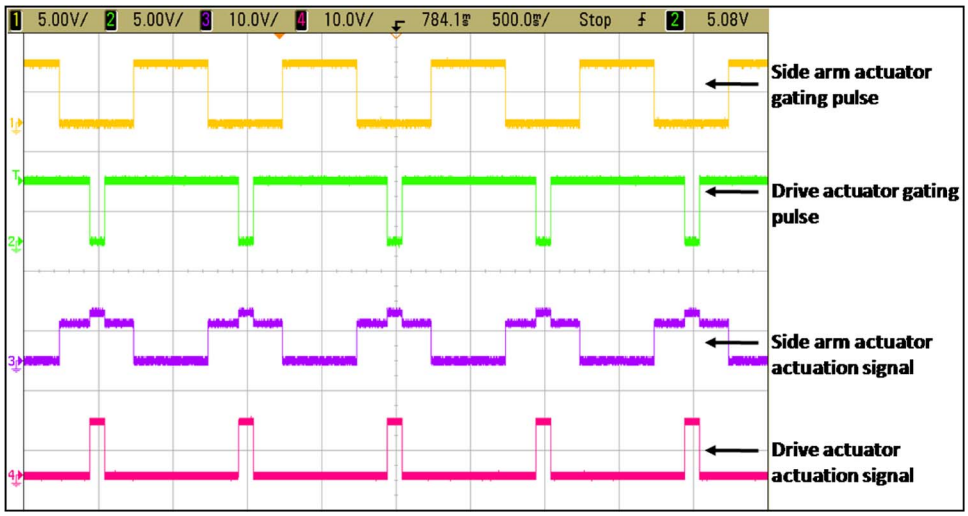


Fig. 12. Oscilloscope screenshot displaying the gating and actuation pulses.

shows the oscilloscope screenshot of the gate signal and actuation signals. The bump in Signal 3 (side arm actuator actuation signal) is due to the crosstalk between the signals (mentioned previously).

To determine the effect of the duty cycle over the bent-beam actuator lifetime, we performed a test in which a chevron actuator (shown in Fig. 13) was put through a series of actuation cycles, but having different duty cycles (20%, 50%, and 80%). The length of the arms for this device was 400 $\mu$m, width of the beams was 2 $\mu$m, and beams were at an angle of 1°. The chevron beams in this actuator were made in the *Poly3* layer which has a thickness of 2.25 $\mu$m and is the same thickness as that of the *Poly4* drive chevron in the bidirectional actuator. A 10 mA current was sourced through the Keithley 2400 source meter, and the duty cycle was controlled using a similar hardware discussed previously. To check the change in material properties of the polysilicon, we monitored the resistance value after every 1–10 cycles, 10–100 cycles in intervals of 10 100 to 1000 cycles in intervals of 100 1000 to 10 000 cycles in intervals of 1000 and 10 000 to 100 000 cycles in intervals of 10 000. The signal characteristics were the same as the signal which was used for the device actuation. Fig. 14 shows the normalized resistance across the actuator after each actuation cycle. After the first actuation, the value of the resistance drops by 1.35% (average) with respect to the original resistance $(R_0)$. The resistance after the 100 000th cycle showed a 1.4% increase for the 20% duty cycle and 1.8% for the 50% duty cycle compared to the resistance measured at the first actuation $(R_1)$. The actuator under test for the 80% duty cycle melted after 60 000 cycles. It was found that there was an increase in resistance of 3.5% after 50 000 cycles with respect to $R_1$. Hence, we conclude that keeping the duty cycle low, i.e., by shortening the "ON" time for a specified frequency, allows the lifetime of an actuator to be extended. Shortening the "ON" times reduces the time period of the heating cycle for the actuator, thus decreasing the annealing time. The increase in resistivity and eventual breakdown shows the degradation in actuator material in devices which were operated 80% duty cycle as compared to that operated at 20% duty cycle. Hence, the decrease in annealing time causes the

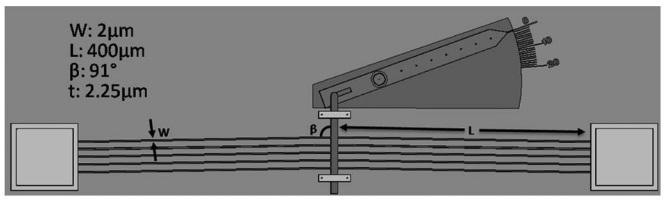


Fig. 13. Top-down view of the chevron actuator used for duty-cycle testing displaying with the parameters shown in the top left.

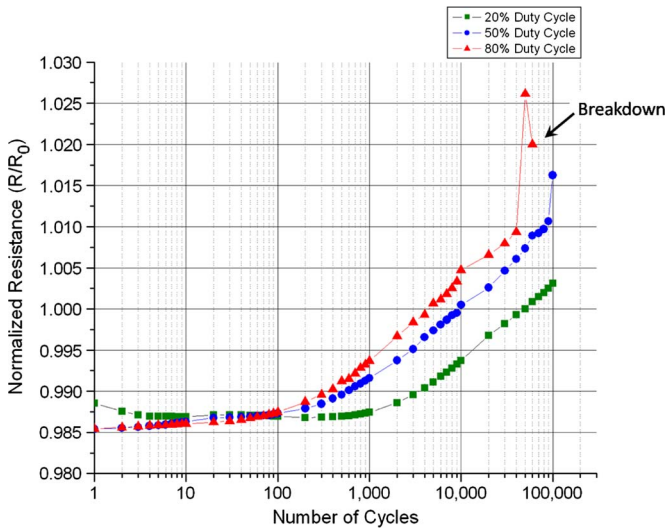


Fig. 14. Plot of normalized resistance v/s number of duty cycles for different duty cycles.

increases in lifetime of the bent-beam actuators. Que *et al.* [28] have determined that the degradation in actuator materials is caused by stress at high operation temperatures. Our results correlate well with the results obtained by Que *et al.*

Fig. 15 shows the captured microscope images (at 20X and 0.4NA) of the device for forward motion at intervals of 5, 10, and 20 actuation events. There is a die defining boundary on the sides of the chip that is constructed on the *Poly2* layer as shown in Fig. 15(d) which restricts off-chip motion of the shuttle. Thus, the maximum number of actuation cycles that can be given to the device for forward motion is currently 20.

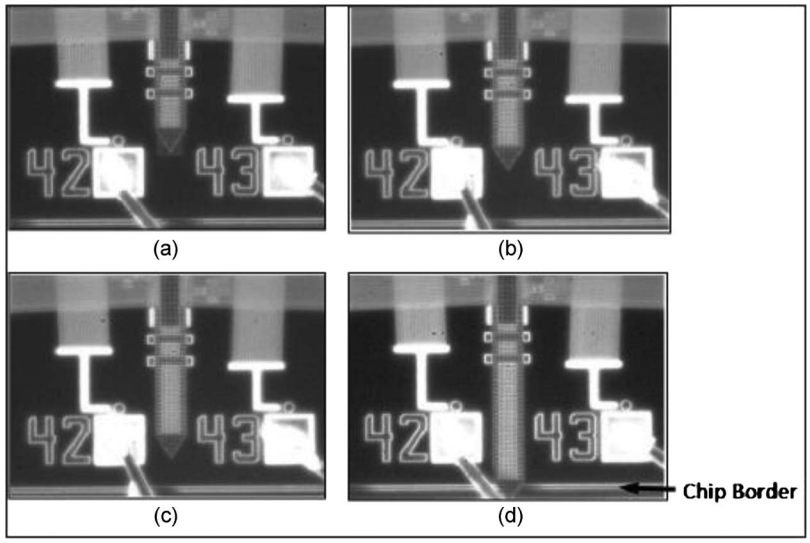


Fig. 15. Microscope images showing the operation of the device in the forward direction. (a) Initial Position. (b) After 5 actuation cycles. (c) After 10 actuation cycles. (d) After 20 actuation cycles.

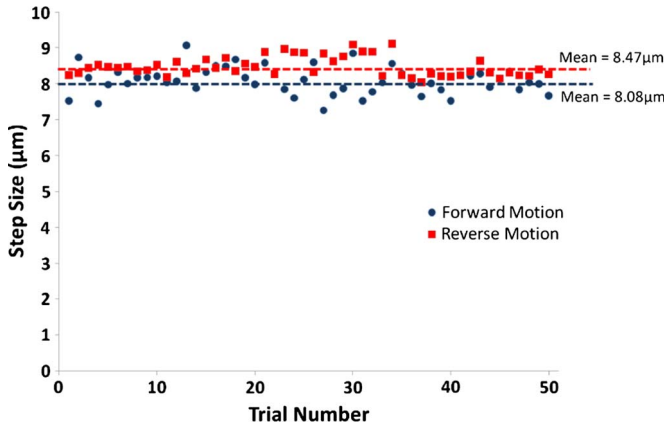


Fig. 16. Displacement of the shuttle for a step size in forward and reverse directions.

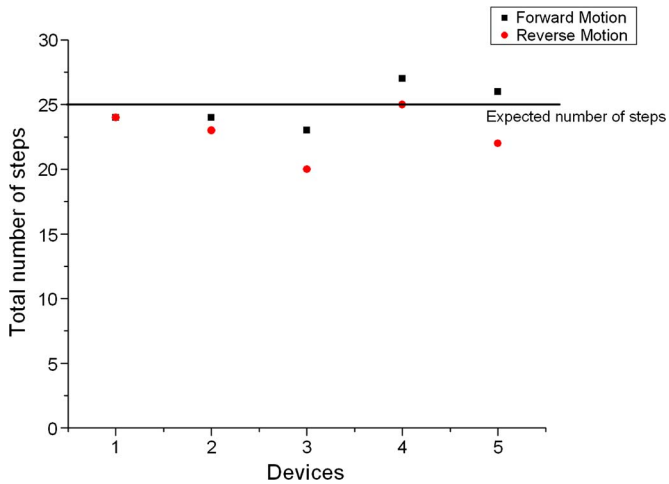


Fig. 17. Total number of steps taken by the device over 25 actuation cycles for forward and reverse motion.

### C. Step Size Determination

A test was done to find the actual step size of the shuttle. Images were captured after the device was powered for one actuation cycle for both forward and reverse steps. Step size determination was done for 50 actuations cycles in both forward and reverse directions. Fig. 16 shows the plot of step size with respect to the trial number. The mean values obtained for step size is $8.5\ \mu\text{m} \pm 0.5\ \mu\text{m}$ reverse and $8.1\ \mu\text{m} \pm 0.5\ \mu\text{m}$ for forward motion. The uncertainty in the step size measurement is primarily due to minimum pixel resolution produced by the optical system. Ideally, the step size should be the design distance between two teeth which is $9\ \mu\text{m}$ for this device as shown in Fig. 3, but another variation in the measurement is due to the free moving shuttle due to the $1\ \mu\text{m}$ clearance between the pawl and the teeth of the shuttle on each side.

### D. Forward and Reverse Steps

In this experiment, tests were carried out to determine the number of steps moved for a given number of actuation cycles and to investigate if there are any missed or extra ratchets. Five actuation cycles were given, and the total number of steps moved by the shuttle was observed for both forward and reverse motion. This was repeated five times for each device, producing 25 steps for each device. The frequency of the actuation pulses was set at 1 Hz, and the duty cycles for the two actuation pulses were 10% and 50% for the drive chevron and side chevrons, respectively. Initial time delay between these two pulses was set at 250 ms. Fig. 17 shows the plot of the number of steps a device took for each 25 step run during its forward motion and backward motion.

### E. Frequency Versus Steps

The same experiment was carried out providing five actuation pulses for different frequencies (1 Hz, 2 Hz, 4 Hz, and 8 Hz). Fig. 18 shows the behavior of the device at different operating frequencies. This test was performed to determine the effect of increasing actuation frequency on the shuttle and determine whether multiple steps per actuation cycle were

occurring. We observed multiple stepping of the ratchet pawl at almost all the tested frequencies. This behavior was more common in the forward motion whereas the skipping events were more prominent for reverse motion. Skipping events occur when the chevron is not able to generate enough force to displace the shuttle by 9 $\mu$m (step size). During the backward motion, displacement is a resultant of force generated by the actuation pulse, whereas forward motion is caused by the energy release which was originally stored in the chevron during its actuation. Some of the force generated in the *Poly4* chevron actuation is used in out-of-plane buckling. It reduces the in-plane displacement of the actuators, and the drive chevron is not able to achieve the step-size displacement required for one step motion. This phenomenon causes the increase in skipping events of the device. The out-of-plane buckling does not noticeably affect the forward direction, as the force generated due to recoil of the chevron is the same as the total force generated in actuation. In comparison to a loaded "torsional ratcheting actuator," where the multiple ratcheting events contribute to the overall momentum of the system, the occurrence of multiple steps in one actuation cycle may be the result of the momentum of DA along with the central shuttle which is resting on dimple structures on the *Poly1* level [29]. Due to process limitations, we were not able to provide an overhanging strap structure for the topmost chevron to restrict out-of-plane motion of the actuator.

Maloney *et al.* observed that when the electrothermal devices were run at frequencies higher than 100 Hz, the displacement amplitude decreases by a factor of 10 for each decade increase in frequency. This displacement drop was attributed to the inability of the heating/cooling cycle for thermal actuator to keep up with the actuation signal. Normally, our device would not be required to run at such high frequencies, but we would expect it to suffer from a similar degradation in performance [30].

The testing of our device demonstrates the successful operation of the bidirectional linear actuator. The displacement of the individual chevron actuators was found to be in accord with the model developed in the FEA tool. The overall power consumption of the device was found out to be $\sim$1 W. The importance of using smaller "ON" times was also studied. The mean step size for forward and reverse motions was obtained as 8.4 $\mu$m and 8.5 $\mu$m, respectively, with an uncertainty of 0.5 $\mu$m. The device was successfully tested at 1 Hz, 2 Hz, 4 Hz, and 8 Hz. It was observed that skipping events increase for the backward motion and the reason for this is attributed to out-of-plane buckling of the drive chevron. The force generated by the system in forward/ backward directions would be the same as that generated by *Poly4* Drive Chevron. Due to limitation of the accurate means to calculate force experimentally, we estimate the force generation analytically by (1) calculated by Que *et al.* using complimentary energy method and is estimated to be 2.9 mN.

## VI. Comparison With Other Devices

Table II consists of dimensional and performance comparison of linear micro-actuators which are reported in the literature. The comparison mainly focuses on three parameters: (i) actuator type, (ii) engine area, and (iii) force. In this comparison, the engine area refers to the footprint of the parts forming the actuator mechanism. In our design, the actuator engine consists of the side actuators and the DA which translates the actuation force provided, into the mechanical motion of the shuttle. We exclude the area required by the shuttle as its dimensions are subject to change depending on the application. Fig. 19 shows the graphical comparison of the generated force with respect to the actuator footprint area. Our work was inspired by the Muthuswamy *et al.* design [1] and includes modifications that allow greater force generation. The engine area was kept roughly the same by stacking up the actuators on different levels and using the same DA for both forward and reverse motions. This utilization of the same actuator for producing bidirectional motion reduces the number of bond pads required for the design. Muthuswamy *et al.* mention that they expect to achieve forces in the range of 100s of $\mu$N which could be increased by adding to the number of arms in the DAs. The area in the plot shows the probable range of force generated by their device. The thermal actuation mechanism provides an edge over the electrostatic microactuation technology because

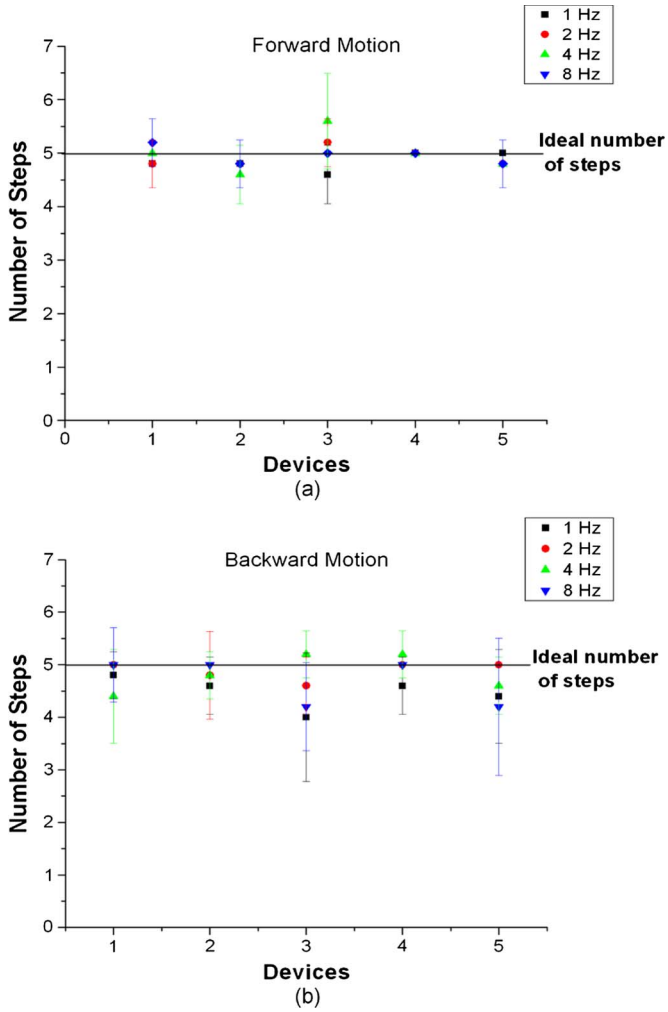


Fig. 18. Number of steps taken by the device at 1 Hz, 2 Hz, 4 Hz, and 8 Hz for all five devices on input of five actuation pulses in (a) forward and (b) backward directions.

TABLE II
DIMENSIONAL AND PERFORMANCE COMPARISON FOR LINEAR MICRODEVICES IN LITERATURE. IN ACTUATOR-TYPE COLUMN, PZ: PIEZO-ELECTRIC, ES: ELECTROSTATIC, AND ET: ELETROTHERMAL ACTUATORS

| | Toda [21 ] | Erismis [9] | Kwon [ 17] | Yeh [11] | de Boer [21] | Pham [12] | Brown [ 20] | Muthuswamy [1] | Arthur [12] | This Work |
|---|---|---|---|---|---|---|---|---|---|---|
| Actuator Type | PZ/ ES | ES | ET | ES | ES | ES | ET | ET | ET | **ET** |
| Engine Area ($mm^2$) | 20.5 | 6 | 0.9 | 0.71 | 0.9 | 0.48 | 0.75 | .32 | .36 | **.34** |
| Force (μN) | 16000 | 110 | 50 | 260 | 450 | - | 138 | 600-1100 (estimated) | 80 | **2760 ±50 (Calculated)** |
| Force/ Area ($N/m^2$) | 780.5 | 18.3 | 55.5 | 366.2 | 500 | - | 184 | - | 222.2 | **8117.6** |

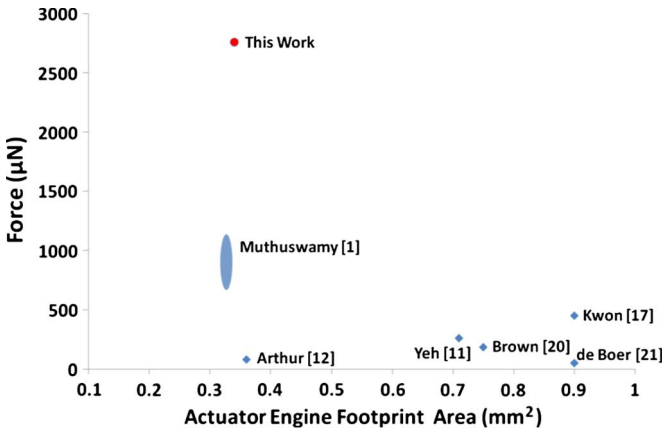


Fig. 19. Graphical comparison of the linear actuators in the literature.

of its low actuation voltages, smaller footprint, and robustness and helps the proposed device operate over a wider range of environmental conditions. In general, our device shows good performance for this class of MEMS.

## VII. CONCLUSION

The multilevel chevron actuator-based positioning system positioning system was successfully designed and fabricated using the SUMMiT V fabrication process. The device was functional for both forward and reverse motion and was verified by means of a custom-built optical characterization setup which was automated using LabVIEW. The device is capable of generating a force of ∼3 mN and presently has a maximum displacement of ∼180 $\mu$m in both forward and reverse directions with a step size of ∼9 $\mu$m. The device is ∼26% smaller and has one fewer bondpad compared to a similar device [1]. The use of a common grounding bondpad causes electrical crosstalk, but it does not compromise the device performance. It is capable of generating greater force because of 22 more arms in the DA in comparison to previous design, and it also utilizes only one actuator system for both forward and backward motions eliminating the need of an extra actuation system making the design more compact. This makes our design more amenable to using multiple devices in an array. In this paper, we demonstrated successful working of this thermal microactuator at various frequencies. This device could enable precise positioning in various applications such as biological cell probing and *in vivo* neural DAQ.

## ACKNOWLEDGMENT

The authors thank Sandia National Laboratories for fabricating, releasing, and packaging the devices used for this work. We acknowledge the help of I. Purushothaman from the Department of Bioengineering, Arizona State University, for contributions to design discussions, and C. Linch, Texas Tech University Health Sciences Center, for the SEM images.

## REFERENCES

[1] J. Muthuswamy, M. Okandan, A. Gilletti, M. S. Baker, and T. Jain, "An array of microactuated microelectrodes for monitoring single-neuronal activity in rodents," *IEEE Trans. Biomed. Eng.*, vol. 52, no. 8, pp. 1470–1477, Aug. 2005.

[2] N. Jackson, P. Stice, M. Okandan, and J. Muthuswamy, "Long-term cortical recordings with microactuated microelectrodes," in *Proc. 3rd Int. IEEE/EMBS Conf. Neural Eng.*, 2007, vol. 1/2, pp. 141–143.

[3] M. Hoffmann, "Techniques in the design and fabrication of optical MEMS switches and their application in optical communication systems," in *MEMS/NEMS Handbook: Techniques and Applications*, vol. 5, *Medical Applications and Moems*. New York: Springer-Verlag, 2006, pp. 181–259.

[4] S. C. Shen, C. T. Pan, and H. P. Chou, "Electromagnetic optical switch for optical network communication," *J. Magn. Magn. Mater.*, vol. 239, no. 1–3, pp. 610–613, Feb. 2002.

[5] L. Fan, M. C. Wu, K. D. Choquette, and M. H. Crawford, "Self-assembled microactuated XYZ stages for optical scanning and alignment," in *Proc. TRANSDUCERS*, 1997, vol. 1/2, pp. 319–322.

[6] D. A. Horsley, N. Wongkomet, R. Horowitz, and A. P. Pisano, "Precision positioning using a microfabricated electrostatic actuator," *IEEE Trans. Magn.*, vol. 35, no. 2, pp. 993–999, Mar. 1999.

[7] V. P. Jaecklin, C. Linder, N. F. de Rooij, and J. M. Moret, "Micromechanical comb actuators with low driving voltage," *J. Micromech. Microeng.*, vol. 2, no. 4, pp. 250–255, Dec. 1992.

[8] Y. Soeno, S. Ichikawa, T. Tsuna, Y. Sato, and I. Sato, "Piezoelectric piggyback microactuator for hard disk drive," *IEEE Trans. Magn.*, vol. 35, no. 2, pp. 983–987, Mar. 1999.

[9] M. A. Erismis, H. P. Neves, R. Puers, and C. Van Hoof, "A low-voltage large-displacement large-force inchworm actuator," *J. Microelectromech. Syst.*, vol. 17, no. 6, pp. 1294–1301, Dec. 2008.

[10] E. Sarajlic, E. Berenschot, N. Tas, H. Fujita, G. Krijnen, and M. Elwenspoek, "High performance bidirectional electrostatic inchworm motor fabricated by trench isolation technology," in *Proc. IEEE TRANSDUCERS*, 2005, vol. 1/2, pp. 53–56.

[11] R. Yeh, S. Hollar, and K. S. J. Pister, "Single mask, large force, and large displacement electrostatic linear inchworm motors," *J. Microelectromech. Syst.*, vol. 11, no. 4, pp. 330–336, Aug. 2002.

[12] P. H. Pham, D. V. Dao, and S. Sugiyama, "A micro transportation system (MTS) with large movement of containers driven by electrostatic comb-drive actuators," *J. Micromech. Microeng.*, vol. 17, no. 10, pp. 2125–2131, Oct. 2007.

[13] C. Arthur, N. Ellerington, T. Hubbard, and M. Kujath, "MEMS earthworm: A thermally actuated peristaltic linear micromotor," *J. Micromech. Microeng.*, vol. 21, no. 3, p. 035022, Mar. 2011.

[14] N. Hubbard and L. Howell, "Experimental repeatability of a thermal actuator for nanopositioning," in *Proc. ASME Int. Mech. Eng. Congr. Expo.*, 2004, pp. 427–432.

[15] J. H. Comtois, M. A. Michalicek, and C. C. Barron, "Characterization of electrothermal actuators and arrays fabricated in a four-level, planarized surfacemicromachined polycrystalline silicon process," in *Proc. Int. Conf. Solid State Sens. Actuators*, 1997, vol. 2, pp. 769–772.
[16] A. D. Oliver, S. R. Vigil, and Y. B. Gianchandani, "Photothermal surface-micromachined actuators," *IEEE Trans. Electron Devices*, vol. 50, no. 4, pp. 1156–1157, Apr. 2003.
[17] L. Que, J. S. Park, and Y. B. Gianchandani, "Bent-beam electrothermal actuators—Part I: Single beam and cascaded devices," *J. Microelectromech. Syst.*, vol. 10, no. 2, pp. 247–254, Jun. 2001.
[18] J. S. Park, L. L. Chu, A. D. Oliver, and Y. B. Gianchandani, "Bent-beam electrothermal actuators—Part II: Linear and rotary microengines," *J. Microelectromech. Syst.*, vol. 10, no. 2, pp. 255–262, Jun. 2001.
[19] H. Kwon, S. Jeong, S. Lee, and J. Lee, "Design and characterization of a micromachined inchworm motor with thermoelastic linkage actuators," *Sens. Actuators A, Phys.*, vol. 103, no. 1/2, pp. 143–149, Jan. 2003.
[20] M. Brown, T. Hubbard, and M. Kujath, "Development of a long-range untethered frictional microcrawler," *J. Micromech. Microeng.*, vol. 17, no. 5, pp. 1025–1033, May 2007.
[21] C. Lee and C. Y. Wu, "Study of electrothermal V-beam actuators and latched mechanism for optical switch," *J. Micromech. Microeng.*, vol. 15, no. 1, pp. 11–19, Jan. 2005.
[22] E. Kolesar, T. Htun, B. Least, and J. Tippey, "Design and performance comparison of single- and double-hot arm polysilicon surface micromachined electrothermal actuators and arrays applied to realize a microengine," in *Proc. 8th IEEE Conf. Nanotechnol.*, Arlington, TX, 2008, pp. 444–447.
[23] M. P. de Boer, D. L. Luck, W. R. Ashurst, R. Maboudian, A. D. Corwin, J. A. Walraven, and J. M. Redmond, "High-performance surface-micromachined inchworm actuator," *J. Microelectromech. Syst.*, vol. 13, no. 1, pp. 63–74, Feb. 2004.
[24] M. V. Shutov, D. L. Howard, E. E. Sandoz, J. M. Sirota, R. L. Smith, and S. D. Collins, "Electrostatic inchworm microsystem with long range translation," *Sens. Actuators A, Phys.*, vol. 114, no. 2/3, pp. 379–386, Sep. 2004.
[25] R. Toda and E. H. Yang, "A normally latched, large-stroke, inchworm microactuator," *J. Micromech. Microeng.*, vol. 17, no. 8, pp. 1715–1720, Aug. 2007.
[26] *SUMMiT V Five Level Surface Micromachining Technology Design Manual*, MEMS Technologies Department, Sandia Nat. Lab., Albuquerque, NM, Version 3.1a, SAND2008-0659, Apr. 2008.
[27] M. S. Baker, R. A. Plass, T. J. Headley, and J. A. Walraven, "Compliant thermo-mechanical MEMS actuators," Sandia Nat. Lab., Albuquerque, NM, Tech. Rep. LDRD #52553, SAND2004-6635, Dec. 2004.
[28] L. Que, J. Park, M. Li, and Y. Gianchandani, "Reliability studies of bent-beam electro-thermal actuators," in *Proc. 38th Annu. IEEE Int. Reliab. Phys. Symp.*, 2000, pp. 118–122.
[29] D. M. Tanner, J. A. Walraven, S. M. Barnes, N. F. Smith, F. Bitsie, and S. E. Swanson, "Reliability of a MEMS torsional ratcheting actuator," in *Proc. 39th Annu. Int. Reliab. Phys. Symp.*, 2001, pp. 81–90.
[30] J. M. Maloney, D. S. Schreiber, and D. L. DeVoe, "Large-force electrothermal linear micromotors," *J. Micromech. Microeng.*, vol. 14, no. 2, pp. 226–234, Feb. 2004.

**Sahil Oak** received the B.E. degree in instrumentation and control engineering from Rajiv Gandhi Technical University, Bhopal, India, in 2007, and the M.S. degree in electrical engineering from Texas Tech University, Lubbock, in 2009, where he is currently working toward the Ph.D. degree in the Microelectromechanical Systems Laboratory.

His research interests include design, modeling, and testing of MEMS and MOEMS with emphasis on material characterization.

**Sandesh Rawool** received the Bachelor of Engineering degree in electronics engineering from the University of Mumbai, Mumbai, India, in June 2006. He received the Master of Science in Electrical Engineering degree from Texas Tech University (TTU), Lubbock, in 2009.

During this period, he worked as a research assistant in the Microelectromechanical Systems Laboratory at TTU on design and characterization of MEMS actuators. Currently, he is working with Texas Instruments Inc., Dallas, TX, as a Test Engineer. His interests include developing test programs and automated test setups for MEMS characterization.

**Ganapathy Sivakumar** received the Bachelor's degree in electronics and communications engineering from Kurukshetra University, Kurukshetra, India, and the Ph.D. degree in electrical engineering from Texas Tech University, Lubbock, in 2010.

He is currently with Texas Instrument Inc., Dallas, TX, where he is a Product Engineer in the DLP Packaging Process Development Group. His research interests include design and modeling of MEMS, developing custom characterization setup for testing of MEMS devices, and characterization of nanoscale/microscale tribological phenomena.

**Egbert J. Hendrikse, Jr.** received the B.S. degree in electrical engineering and the Masters, and Ph.D. degrees in industrial engineering from Texas Tech University, Lubbock, in 2007, 2008, and 2011, respectively.

He is currently working at Texas Instruments, Attleboro, MA, as a human factors and ergonomics specialist. His interests include applying human factors and ergonomic principles to product and task design.

**Daniel Buscarello** received the B.S. degree in electrical engineering from Texas Tech University, Lubbock, in 2007.

He is currently working at B&W Pantex in Amarillo, TX, as an Electrical and Software Engineer. His interests include developing workstations with integrated instruments and customizing user interfaces to control them.

**Tim Dallas** (M'00) received the B.A. degree in physics from the University of Chicago, Chicago, IL, and the M.S. and Ph.D. degrees in physics from Texas Tech University, Lubbock.

He is an Associate Professor of Electrical and Computer Engineering at Texas Tech University. His research includes MEMS packaging issues with an emphasis on stiction. In addition, his research group designs and tests SUMMiT processed dynamic MEMS devices including micropositioners and micromirrors. The MEMS group at Texas Tech has strong education and outreach efforts in MEMS and has developed a MEMS education chip for use in wide range of educational settings. This technology is commercially available from his start-up company, Class on a Chip, Inc. He worked as a Technology and Applications Engineer for ISI Lithography and was a Postdoctoral Research Fellow in chemical engineering at the University of Texas, prior to his faculty appointment at TTU.